Helmholtz-Zentrum Dresden-Rossendorf (HZDR)

HELMHOLTZ ZENTRUM
DRESDEN ROSSENDORF

TiAl-based semi-finished material produced by reaction annealing of Ti/Al layered composite sheets

Pukenas, A.; Chekhonin, P.; Scharnweber, J.; Chulist, R.; Oertel, C.-G.; Freudenberger, J.; Skrotzki, W.;

Originally published:

December 2021

Materials Today Communications 30(2022), 103083

DOI: https://doi.org/10.1016/j.mtcomm.2021.103083

Perma-Link to Publication Repository of HZDR:

https://www.hzdr.de/publications/Publ-33901

Release of the secondary publication
on the basis of the German Copyright Law § 38 Section 4.

CC BY-NC-ND

TiAl-based semi-finished material produced by reaction annealing of Ti/Al layered composite sheets

A. Pukenas[1], P. Chekhonin[2], J. Scharnweber[1], R. Chulist[3], C.-G. Oertel[1], J. Freudenberger[4,5], W. Skrotzki[1*]

[1] Institut für Festkörper- und Materialphysik, Technische Universität Dresden, 01062 Dresden, Germany

[2] Helmholtz-Zentrum Dresden-Rossendorf, Bautzner Landstrasse 400, 01328 Dresden, Germany

[3] Institute of Metallurgy and Materials Science, Polish Academy of Sciences, 25 Reymonta St, 30-059 Cracow, Poland

[4] Leibniz-Institut für Festkörper- und Werkstoffforschung Dresden (IFW Dresden), Helmholtzstr. 20, 01069 Dresden, Germany

[5] Institut für Werkstoffwissenschaft, TU Bergakademie Freiberg, Gustav Zeuner Str. 5, 09599 Freiberg, Germany

* Corresponding author

E-mail address: werner.skrotzki@tu-dresden.de (W. Skrotzki)

Abstract

In this study multi-layered Ti/Al sheets prepared by accumulative roll bonding (ARB) underwent a two-step heat treatment (HT) to form intermetallic compounds. The microstructure and crystal structure of the samples were examined by scanning and transmission electron microscopy as well as energy-dispersive X-ray spectroscopy and synchrotron diffraction. In the first solid-state reaction annealing step, Ti-rich ARB samples containing 60 at.% Ti and 40 at.% Al were held at 600°C for 12 h under a uniaxial pressure between 0 MPa and 50 MPa applied along the normal direction of the sheets. At this stage, Al is completely consumed by forming mainly Al-rich intermetallic phases and to a lower extent other titanium aluminides such as Ti_3Al and TiAl. In the second step, high-temperature annealing produces TiAl and Ti_3Al as major phases during both pressureless annealing at 1100°C, 1200°C and 1300°C and annealing under an uniaxial pressure of about 100 MPa at 1200°C. Pore formation during the reaction annealing can be significantly reduced by the applied pressure. As a result, a TiAl-based semi-finished material was fabricated.

1. Introduction

Titanium aluminides have attracted much interest because of their potential as engineering materials. High melting points, low density, excellent creep strength and good corrosion resistance [1, 2, 3] make them beneficial for use in automobile (exhaust valves, turbocharger wheels [4, 5]) and aerospace (compressor vanes, turbine blades, turbine exhaust components [6, 7, 8]). Within the Ti-Al system, there are two titanium aluminides of industrial importance. The compounds are Ti_3Al and TiAl with hexagonal $D0_{19}$ and tetragonal $L1_0$ structure, respectively. Due to planar slip, limited number of slip systems and lack of twinning they exhibit low ductility in the binary state [9, 10]. Various alloys based on Ti_3Al and TiAl have been developed [11, 12]. Of special interest for commercial applications are two-phase TiAl/Ti_3Al alloys consisting of duplex or fully lamellar microstructure [13, 14], which is controlled by both, the heat treatment process and the chemical composition.

The processing of Ti aluminides includes various methods, such as ingot metallurgy [15], powder metallurgy [16, 17], selective laser melting [18], explosive welding [19] or electron beam melting [20]. Solid-state reaction annealing of Ti and Al foils has been also used for manufacturing of near-net-shaped sheets [21, 22, 23]. In general, high defect densities imposed by large strain plastic deformation and fine layering can enhance the transformation to desirable phases. Amongst different severe plastic deformation methods, accumulative roll bonding (ARB) is an effective method to produce multilayered ultra-fine grained Ti/Al layered composites [24, 25]. However, during subsequent reaction annealing steps of Ti/Al diffusion couples, pore formation takes place. Hot-rolling or pressure-assisted methods have been reported to reduce porosity [21, 26].

In this study, it was the aim to fabricate sheet profiles from ARB-processed Ti/Al sheets which after reaction annealing only consist of TiAl and Ti_3Al. To achieve this, a two-step reaction annealing (heat treatment, HT) without and with uniaxial pressure was applied. HT below the melting point of Al (HT1) prevents the Al from melting and squeezing out, thus the whole Al can be consumed completely for the formation of intermetallic phases. Additional HT at high temperatures (HT2) is necessary to transform the composite of Ti and titanium aluminides to the desired final phase composition.

2. Experimental

Laminates of Al alloy AA5049 (in the following referred to as Al) and high purity Ti (99.995 %) were produced by ARB at RT up to 8 cycles with intermediate annealing steps. A sandwich of two Ti and one Al layer in between with a thickness of 1 mm each and two additional Al layers with a thickness of 0.5 mm placed on top and bottom was stacked

resulting in a 50 vol.% Ti and 50 vol.% Al initial composition. The stack was rolled to a thickness reduction of 50% and halved in length. Both sheets were stacked and rolled again to a thickness reduction of 50%. The cutting, stacking and rolling procedure was repeated to accumulate the strain and reduce the layer thickness. Between each ARB cycle annealing was performed at 450°C for 1 h. More details on the ARB process and sample design are given in [24, 25].

The Ti/Al composite sheet was cut by electrical discharge machining into small pieces (typically about 0.5 cm^2). For the first heat treatment (HT1: 600°C, 12 h) the furnace was evacuated to about 10^{-2} mbar four times and backfilled with Ar in between. Moreover, to avoid sample oxidation, the samples were enclosed in a 0.04 µm thick stainless steel foil. The steel foil package also included some pieces of Nb-foil used as an indicator of oxidation. The HT temperatures were achieved with a heating rate of 300 K h^{-1}. After HT the samples were furnace cooled to RT with a cooling rate of about (100 - 150) K h^{-1}. To reduce porosity formation during HT1 uniaxial pressures up to 50 MPa have been applied. The uniaxial pressure in the furnace was applied with a constant load. Due to geometric changes the true pressure on the samples was noteworthy reduced in comparison with the nominal pressure at the start of heat treatment.

For the second heat treatment, a series of experiments was carried out for 12 h with no external load being applied at 1100°C, 1200°C and 1300°C in order to determine the optimum temperature for this reaction stage. To protect against oxidation, the samples were enclosed in quartz ampoules, which were then evacuated and filled with pure argon gas.

The second heat treatment under pressure was realized with a self-made pressure assembly shown in Fig. 1. It consists of two screws and a nut fabricated with electrical discharge machining from Ni-based superalloy PM 3030 [27]. The samples were placed between two high-temperature ceramic spacers or hemispherical punches with pre-shaped curvature. By tightening the screws at both ends of the nut, a uniaxial pressure is exerted. This assembly ensures only a rough estimate of the pressure due to thermal expansion and lack of exact friction coefficients. Nevertheless, this technique can show the effect of pressure on the formation of porosity.

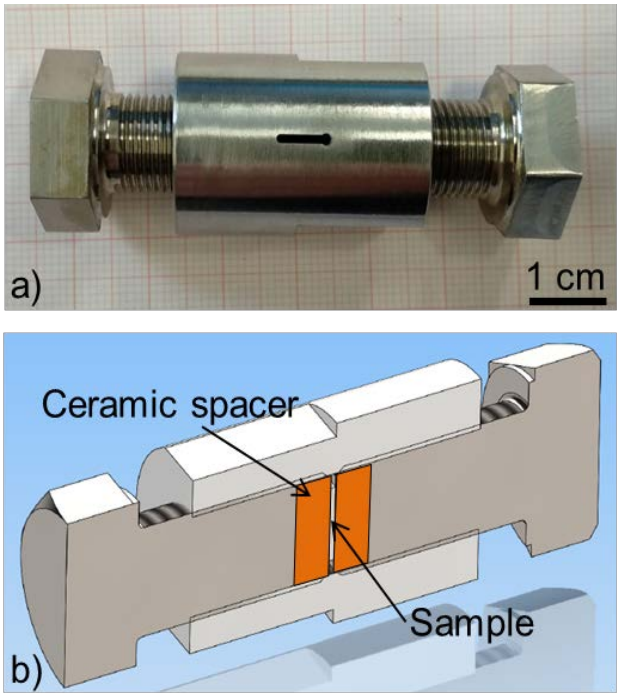

Fig. 1: (a) Pressure assembly, (b) cross-section schematic of the pressure assembly.

Cross-sections of the samples were mechanically wet ground with SiC paper of grit size 1000 - 4000. For scanning electron microscopy (SEM), a 3 h vibration polishing was applied using a polishing cloth (MicroCloth/Buehler) in combination with 0.05 µm alumina suspension (MasterPrep/Buehler). The final polishing step for 30 min took place with MicroCloth and MasterMet (Buehler) 0.02 µm SiO_2 suspension. This preparation is sufficient for SEM imaging of heat-treated samples. For EBSD and for SEM imaging of the initial sheets, instead of vibration polishing the samples underwent electropolishing using 9 vol.% perchloric acid in 91 vol.% ethanol at a voltage of 33 V. The polishing agent was externally cooled to - 20°C. Additionally, the samples were cooled in liquid nitrogen just before electropolishing.

Microstructural investigations were carried out in an ULTRA 55 (Zeiss) SEM equipped with an electron backscatter diffraction (EBSD) system (HKL Technology) and an energy dispersive X-ray spectroscopy (EDX) detector (Bruker). Secondary electron (SE) and backscatter electron (BSE) imaging, as well as EBSD and standardless EDX measurements, were done on the plane normal to the transverse direction (TD).

For one selected specimen standardless EDX was also performed in an FEI Tecnai T20 transmission electron microscope (TEM) equipped with a LaB_6 cathode operated at an acceleration voltage of 200 kV. Specimen preparation for TEM was done by focused ion beam (FIB) technique in a FEI Helios 600i FIB on the rolling direction (RD) plane.

The phase analysis was done using high-energy (λ = 0.01423 nm) synchrotron radiation X-ray diffraction (SR-XRD). The SR-XRD experiments were carried out in transmission geometry at DESY, Hamburg, Germany. The samples were rotated around an axis (RD or TD) perpendicular to the incident beam. The intensity was integrated over the whole Debye rings and the resulting patterns of the Ti-aluminide phases were analyzed with the Rietveld refinement method using HighScore Plus software and the so-called continuous mode for synchrotron diffraction [28, 29]. Such a procedure practically reduces the effect of crystallographic texture allowing very precise calculations of the volume fraction.

To estimate the pore volume fraction, the porosity was quantitatively analyzed from SEM images. Several images were taken in the mid-section of the samples covering an area of 75×52 µm² (HT1 at 600°C and HT2 at 1100°C) and 365×250 µm² (HT2 at 1200°C and 1300°C). The porosity was measured with the line intersection method.

3. Results

3.1 Characterization of the initial material

As shown in Fig. 2 (diffraction pattern at the bottom), only intensity peaks of Al and Ti were measured by SR-XRD. Besides of Ti and Al phases, a few low intensity peaks were observed most likely as a result of precipitation in Al. Thus, it can be concluded that within the detection limit of less than 1 vol.% a reaction of Al and Ti to intermetallic phases did not occur during the ARB process.

Figure 3a shows the SEM cross-section image of a Ti/Al composite sheet after eight ARB cycles. The dark and bright layers in the image represent Al and Ti, respectively. They are continuous and pore-free; the interfaces between Ti and Al are wavy. As the Ti layers experience some minor necking their thickness varies typically between ≈1 µm and ≈10 µm. The average layer thickness is roughly 5 µm. The phase structure of the initial ARB material as given by both the Rietveld and SEM image analysis stands at 62 vol.% for Ti and 38 vol.% for Al, corresponding to 60 at.% Ti and 40 at.% Al. Alloying elements in the Al alloy are neglected. The ARB process results in a change of the initial Ti/Al composition. On the one hand, this is because there is always an Al layer on the outside after each ARB cycle, and wire brushing, therefore, causes some Al removal on these surfaces. On the other hand, Al is squeezed out during ARB processing.

In the dark Al layers numerous evenly distributed bright grains of the size up to several µm were observed (Fig. 3b). They represent Al containing precipitates with a higher atomic number than the surrounding matrix. Analysis of the chemical composition carried out by

SEM EDX shows that the precipitates are rich in Mg, Mn, Fe Ti and Si (also detected in precipitates not shown in Fig. 3b), which are the main alloying elements of AA5049.

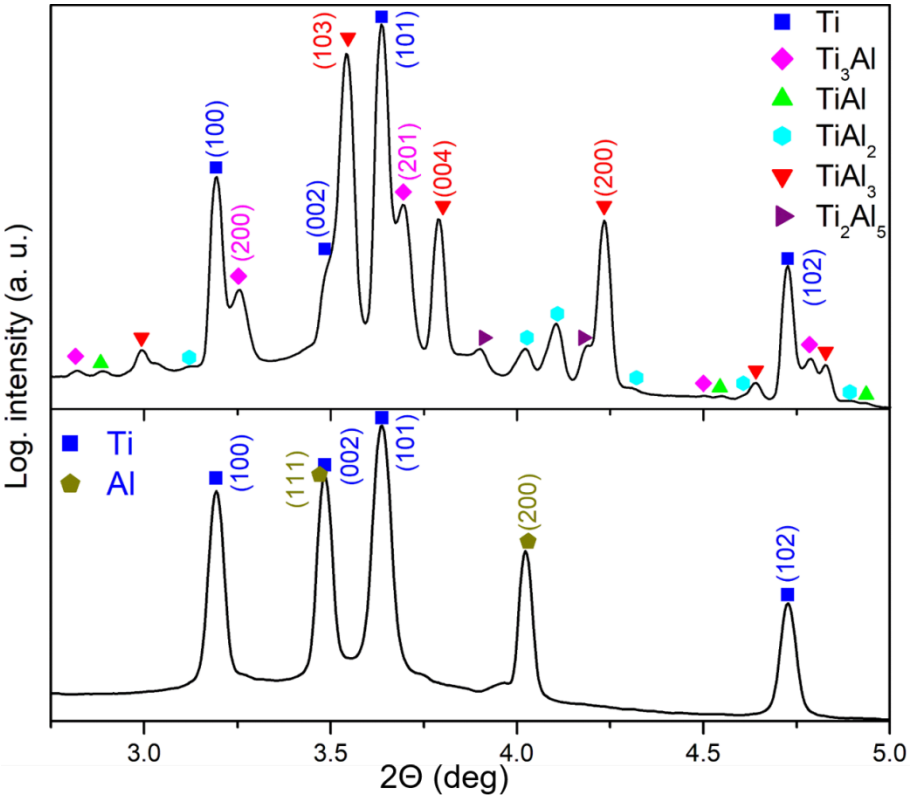

Fig. 2: SR-XRD patterns of Ti/Al ARB material before (lower pattern) and after 12 h HT at 600°C/0 MPa (upper pattern). Observed peaks are indexed to: Ti (hexagonal, P63/mmc); Al (cubic, Fm-3m); Ti_3Al (hexagonal, P63/mmc), TiAl (tetragonal, P4/mmm); $TiAl_2$ body-centered tetragonal I41/amd); $TiAl_3$ (body-centered tetragonal, I4/mmm), Ti_2Al_5 (tetragonal, P4/mmm). Only the intense peaks are labelled.

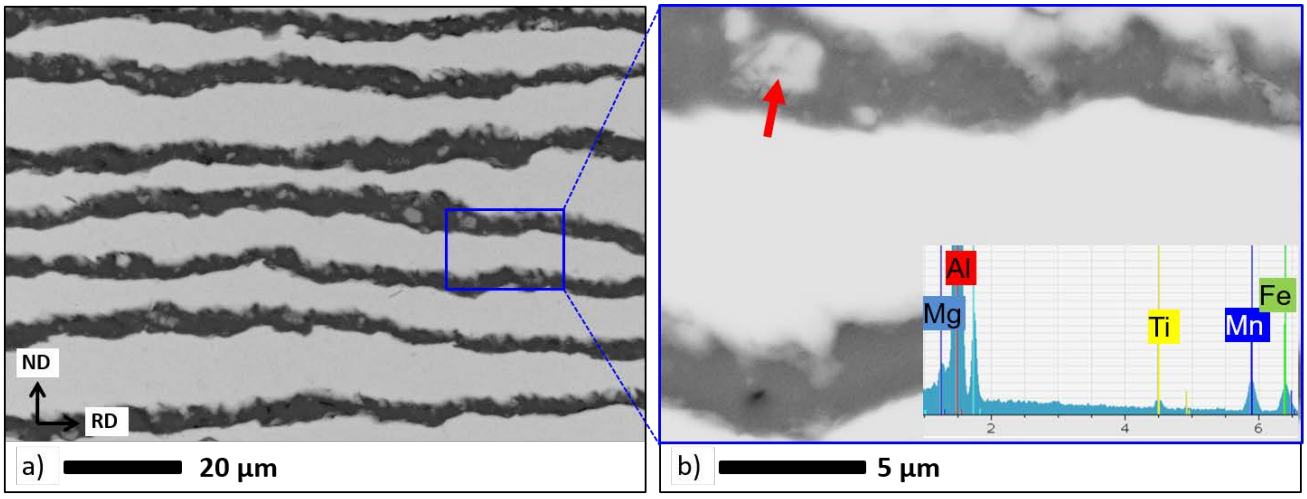

Fig. 3: a) SEM BSE image showing the transverse section of an as-ARB Ti/Al composite sheet: Bright layers correspond to Ti dark layers to Al. Porosity is absent in this condition. b) Magnified image of a) (blue square). The inset in b) shows a typical EDX spectrum obtained from the precipitates in the Al layers (red arrow).

3.2 First heat treatment stage (HT1)

Samples heat-treated at 600°C changed their dimensions and often lost their original rectangular shape. For example, the length of the sample heat-treated without pressure increased by about 5% in TD and RD while the increase in the normal direction (ND) amounted to 12%. This anisotropy may be qualitatively understood by the nearly parallel alignment of the Ti layers providing some constraint to the layered composite to expand in RD and TD during the reaction. This change is different for samples annealed with pressure. For example, for the 600°C/30 MPa sample, the increase is about 8% and 9% in RD and TD, respectively, while in the direction of pressure (ND) there is a thickness decrease of about 10%.

Figure 2 exemplarily shows the SR-XRD pattern (upper pattern) for the 600°C/0 MPa sample. The absence of Al peaks and the appearance of additional diffraction peaks compared to the initial material prove the complete consumption of Al during the formation of intermetallic layers. Basically, after the first reaction treatment, Ti and five intermetallic compounds, Ti_3Al, TiAl, $TiAl_2$, $TiAl_3$ and Ti_2Al_5, are present with $TiAl_3$ and residual Ti dominating. Figure 4 shows volume fractions of the phases calculated using quantitative phase analysis by Rietveld refinement. The refinement reveals that with increasing load more Ti is consumed, i.e., from 36 vol.% at 0 MPa to 28 vol.% at 50 MPa, whereas the major phase $TiAl_3$ increased from 45 vol.% to 55 vol.%. The amounts of Ti_3Al, TiAl, $TiAl_2$ and Ti_2Al_5 are below 12 vol.%.

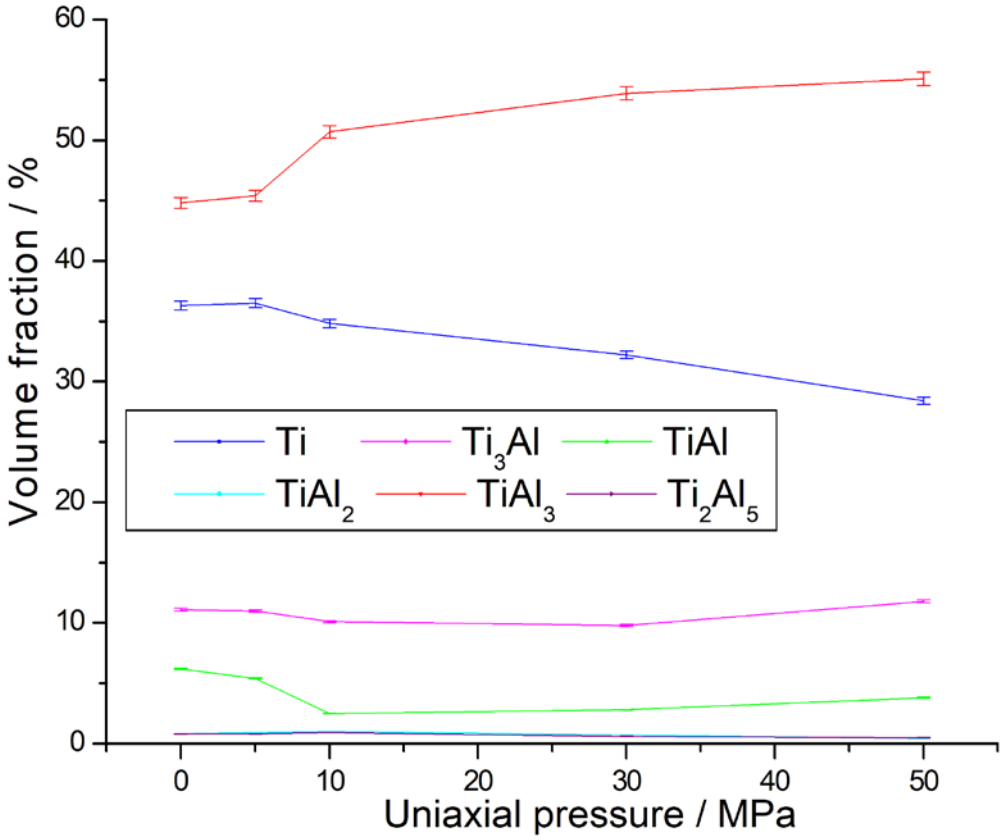

Fig. 4: Volume fraction of Ti and Ti aluminides after HT1 as a function of uniaxial pressure (as determined from Rietveld analysis).

Figure 5 compares the resulting microstructures of the heat-treated ARB samples under different pressure conditions. The microstructures exhibit a small amount of porosity and at least two distinct phases: the bright Ti-rich and the dark Al-rich layered phases. According to SEM EDX, the dominating dark grey layers correspond to $TiAl_3$ (25.2 at.% Ti and 74.8 at.% Al) and the bright grey layer to Ti. For different pressures, the most noticeable differences are the flattening of the layers and the porosity. Longitudinally extended pores are located in the former Al layers. In general, two types of porosity can be distinguished. The first consists of coarse pores, typically located in the $TiAl_3$ layer appearing very notable in Figs. 5a, b. These pores are significantly reduced after the application of pressure and disappear at pressures ≥ 10 MPa. However, independent of pressure another type of fine pores exists (Figs. 5c, d). The fine pores are mainly located to a narrow stripe in the centre of the $TiAl_3$ layers and often appear at triple junctions of the ultra-fine grains.

Figure 6 shows the effect of uniaxial pressure on the porosity during HT1. Without application of pressure, the porosity is about 12 vol.%. At 5 MPa and above it decreases to about 1 vol.%.

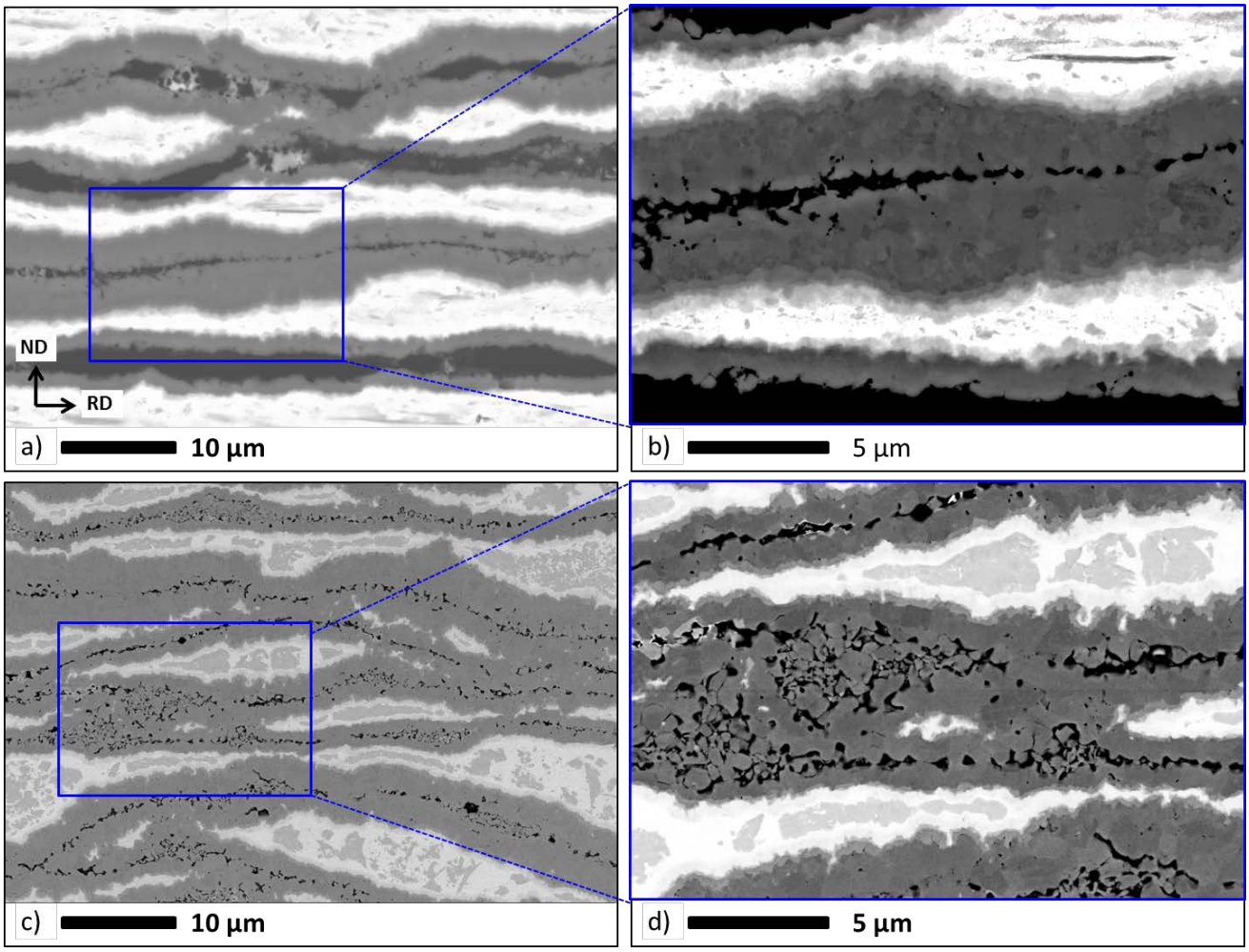

Fig. 5: SEM BSE images of heat-treated samples (600°C/ 12 h) for zero pressure (a and b) and 50 MPa (c and d). Bright grey layers correspond to Ti, dark grey layers to Al, black areas are pores.

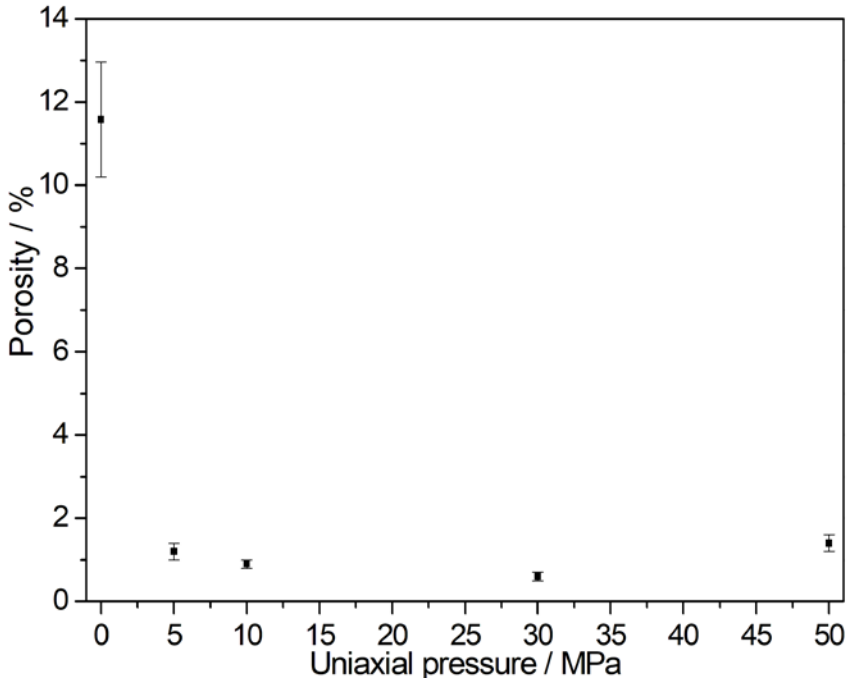

Fig. 6: Porosity given as volume fraction as a function of uniaxial pressure during HT1.

The interface between Ti and $TiAl_3$ is too narrow to be reliably analyzed by SEM EDX. Therefore, TEM EDX was used to determine the composition profile of the interfacial region in the 600°C/5 MPa sample. Figure 7a shows a cross-sectional scanning transmission electron microscopy (STEM) image with a pink line marking the trace of the EDX line scan. The line scan starts in a Ti layer, crosses the three additional layers and ends in a $TiAl_3$ layer. The different layers are not easily distinguishable as the orientation contrast sometimes outweighs the contrast from the different phases. The evaluation of the measured spectra is presented in Fig. 7b. A gradual increase of the Al concentration can be observed along the line scan. Clear plateaus with constant concentration are typically missing. This may be explained by the uneven reaction interface between Ti and $TiAl_3$ leading to an EDX signal originating from volume overlap of different phases along the beam direction. However, it appears that 5 regions can be distinguished: Ti, Ti_3Al, TiAl, $TiAl_2$ and $TiAl_3$.

The reaction between Ti and Al can also be observed in Fig. 7c. It shows gradually increasing contrast from left to right across the layers corresponding to the phase sequence Ti-Ti_3Al-TiAl-$TiAl_2$-$TiAl_3$. The SEM BSE images and EDX measurements do not reveal the Ti_2Al_5 phase.

The microstructure evolution during HT1 was also studied by EBSD. As shown in Fig. 7d, two of the layers could be indexed: Ti_3Al was indexed using the same hexagonal EBSD match unit as for Ti. In the EBSD mapping, the Ti_3Al phase is manually colored blue, assuming that the small grains at the border of Ti are belonging to Ti_3Al, in agreement with SEM and TEM investigations. The $TiAl_2$ was indexed with a cubic match unit. Evidently, initially after 8 ARB cycles, fine-grained Ti is recrystallized throughout most of the layer during HT1. The grains in $TiAl_3$ have an average grain size of about 1 µm, while in Ti_3Al and $TiAl_2$ the grain size is typically below 1 µm. The very thin layer between Ti_3Al and $TiAl_2$ (presumably TiAl) could not be indexed by EBSD. Additionally, the pores inside the $TiAl_3$ layer significantly increased their size after electropolishing, making indexation impossible.

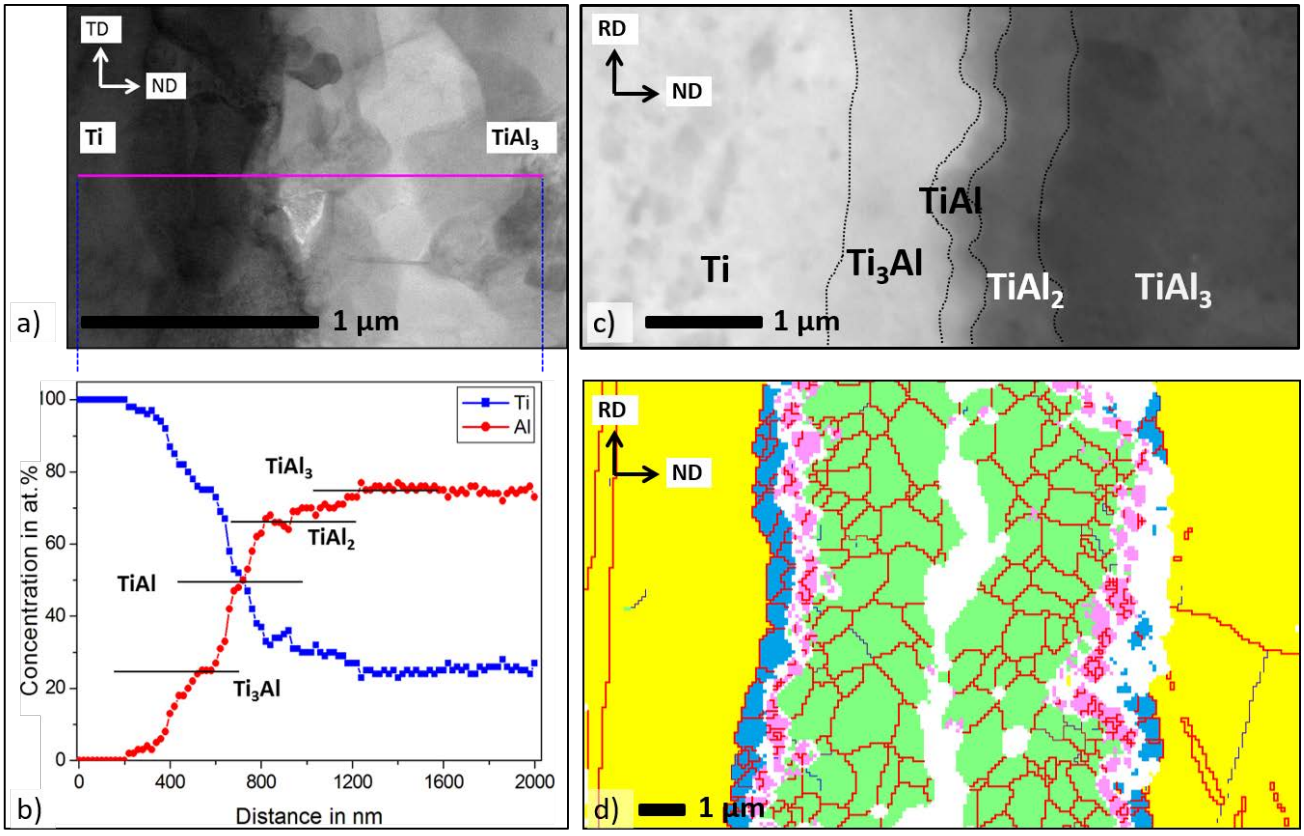

Fig. 7: a) Bright-field STEM image with pink line marking the EDX line scan. b) The concentration of Al and Ti along the pink line. c) SEM BSE contrast image showing the former interface between Ti and Al layers after 600°C/5 MPa HT1. c) EBSD phase mapping with colors assigned as: Ti - yellow, Ti_3Al - blue; $TiAl_2$ - pink, $TiAl_3$ - green. High angle grain boundaries (misorientation >15°) are drawn in red, low angle grain boundaries (misorientations between 2° and 15°) in blue. White areas are not indexed.

3.3 Second heat treatment stage (HT2)

All samples after the second heat-treatment at 1200°C and 1300°C without pressure (prior HT1: 10 MPa and 30 MPa) are weakly convex and exhibit the formation of an oxide/reaction scale of about (10 - 200) µm thickness. The oxide/reaction scale formed on a sample after 1300°C HT2 appeared to be thicker than those on samples after HT2 at lower temperatures.

Figure 8 shows SR-XRD patterns obtained from samples after HT2. The pattern at the bottom is from an 1100°C HT2 sample which contains mainly TiAl and Ti_3Al, but also a slight amount of $TiAl_2$. At higher temperatures, all Al-rich phases have already transformed into TiAl and Ti_3Al. The main peaks in specimens reactively treated at 1200°C and 1300°C are identified as TiAl and Ti_3Al (upper pattern in Fig. 8, exemplarily shown only for 1200°C/0 MPa HT2). In addition to peaks of intermetallic phases, peaks of oxide phases α-Al_2O_3 and Ti_2O_3 can be observed.

Figure 9a shows the cross-section image after HT2 (1100°C/0 MPa) of a sample that underwent HT1 (600°C/30 MPa). The microstructure is characterized by a layered structure of three intermetallic phases and pores (1.2 ± 0.1 vol.%) distributed inside the dark and grey layers. According to EDX, the bright phase appears to have the stoichiometry of Ti_3Al (76.5 at.% Ti, 23.5 at.% Al), the grey phase that of TiAl (48.4 at.% Ti, 51.6 at.% Al) and the dark phase that of $TiAl_2$ (33.9 at.% Ti, 66.1 at.% Al). Aside from slight coarsening of pores, it seems that the porosity is kept to a similar extent from HT1.

HT2 at 1200°C was done on samples, which previously underwent HT1 at pressures of 10 MPa and 30 MPa. The effect of pressure on pore reduction in samples heat-treated at 1200°C is demonstrated in Figs. 9b, c. The porosity has decreased from about 4.3 vol.% (no pressure applied, Fig. 9b) to less than 0.4 vol.% (≈ 100 MPa, Fig. 9c). The microstructure of both samples consists of a matrix of TiAl phase with Ti_3Al islands (bright grains) and lamellar grains composed of alternating plates of TiAl and Ti_3Al. As proven by EDX analysis, the bright grains consist of 63.6 at.% Ti and 36.5 at.% Al, the dark ones of 54.1 at.% Ti and 45.9 at.% Al. Considering the accuracy of standardless EDX, these values correspond to the stoichiometry of Ti_3Al (range of homogeneity domain x_{Al} = 0.20 - 0.38) and TiAl (range of homogeneity domain x_{Al} = 0.47 - 0.62 [30]), respectively.

Figure 9d shows the resulting microstructure after HT2 at 1300°C without pressure. Compared to previous samples, the size of the lamellar TiAl/Ti_3Al colonies is increased. The microstructure also exhibits linearly distributed Ti_3Al grains surrounded by TiAl phase. Furthermore, a number of much smaller Ti_3Al grains is located along the previous ARB interfaces. EDX analysis yields 69.4 at.% Ti and 30.6 at.% Al, and 51.4 at.% Ti and 48.8 at.% Al for bright and dark grains, respectively. The porosity is about 3.8 vol.%.

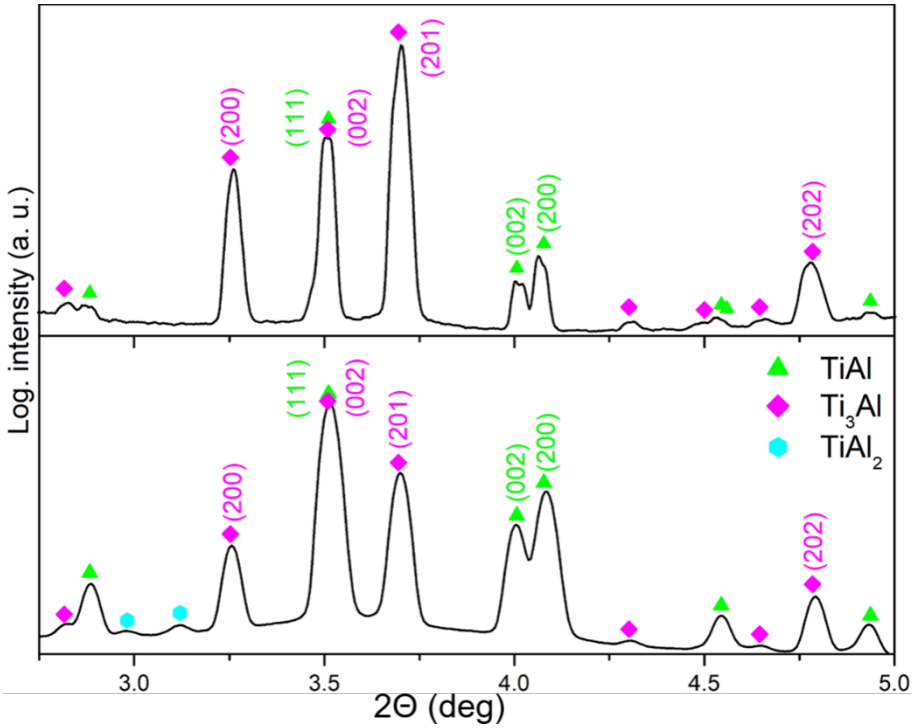

Fig. 8: SR-XRD patterns obtained from samples after HT2 at 1100°C (HT1: 600°C/30 MPa) (lower pattern) and at 1200°C (HT1: 600°C/10 MPa) (upper pattern). Only the intense peaks are labelled.

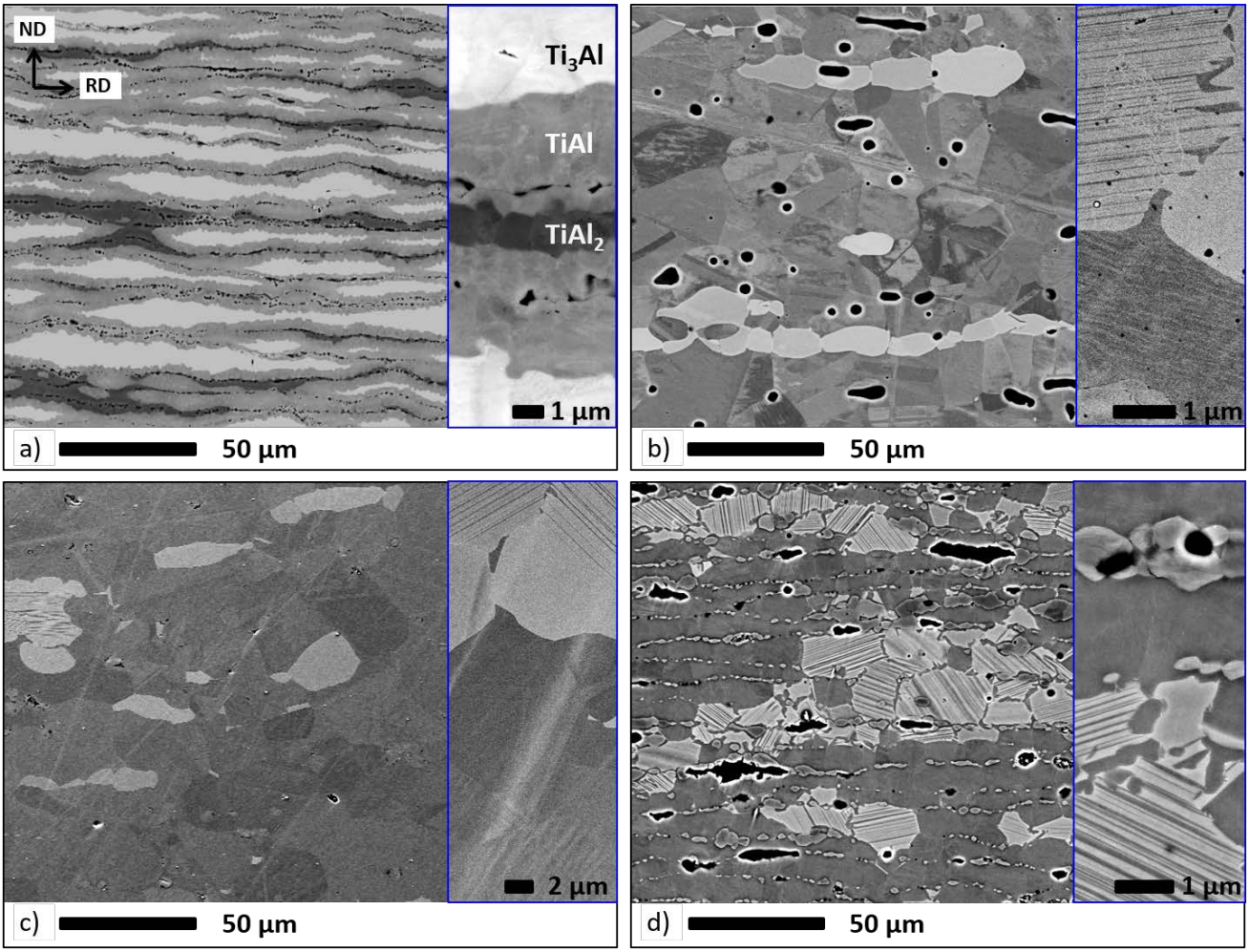

Fig. 9: SEM BSE contrast images of samples after HT2 taken in the centre of cross section: a) HT1: 600°C/30 MPa, HT2: 1100°C/0 MPa; b) HT1: 600°C/10 MPa, HT2: 1200°C/ 0 MPa; c) HT1: 600°C/30 MPa, HT2: 1200°C/≈100 MPa; d) HT1: 600°C/10 MPa, HT2: 1300°C/0 MPa. The insets show the microstructure at higher magnification.

3.4 Fabrication of an intermetallic sheet profile

In the case of ARB Ti/Al sheet profile, the compressive stress required for curved shape formation was introduced by using a self-made jig containing a die into which the negative shape anvil is pressed. The Ti/Al sheet deformation was performed at RT before HT1. Figure 10a shows a pre-shaped Ti/Al sheet after bending to a radius of 8.8 cm. Such a shape would be difficult to obtain at low temperatures from an intermetallic sheet due to its high brittleness. Compared to the as-ARB sheet after bending the Al-layers on the cross-section surface contain material outbreaks (Fig. 10b), the reason will be discussed below. Nevertheless, the microstructure and porosity (2.2 ± 0.4 vol.%) after HT1 (Fig. 10c) and HT2 (Fig. 10d) are comparable to that of the flat sheets (Figs. 5c, 9c). The remaining porosity after HT2 is 0.3 ± 0.1 vol.%.

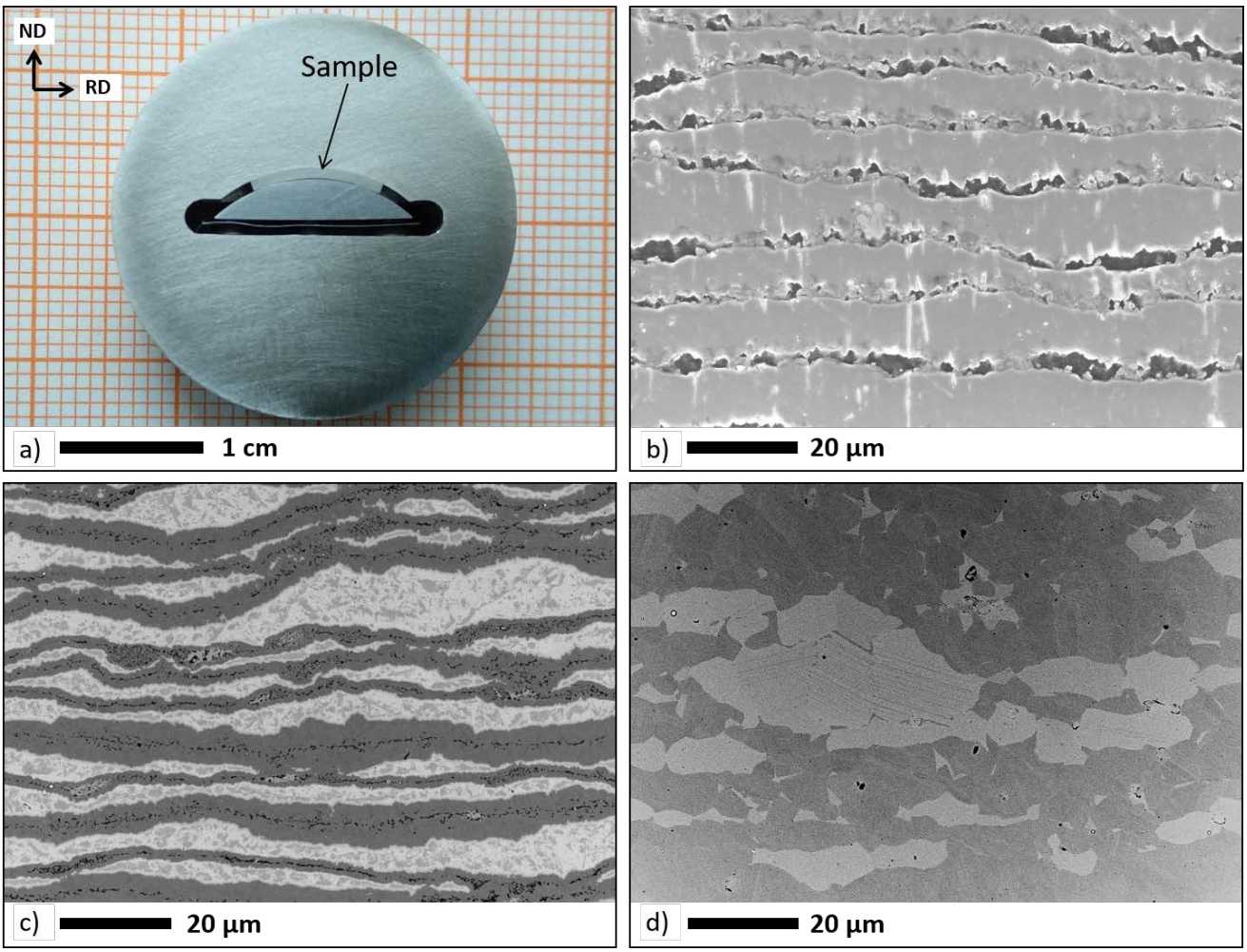

Fig. 10: a) Profile of an ARB sheet bent at RT. b) SEM SE contrast image showing microstructure after RT deformation. Dark areas in the Al layers represent material outbreaks. SEM BSE contrast images of microstructures after heat treatment: c) HT1 (600°C/30 MPa) and d) HT2 (1200°C/≈100 MPa).

4. Discussion

4.1 Phase formation

From a manufacturing perspective, the chosen heating duration and temperature can be further optimized. There have been numerous studies on the formation of Ti aluminides by solid-state reaction [21, 22, 26, 31]. Based on these studies, the first heat treatment temperature was chosen to be 600°C. Heat treatment at higher temperatures increases the diffusivity. However, temperatures closer to the melting point of Al during HT1 under uniaxial pressure are not expedient since the flow stress of Al strongly decreases and Al layers may squeeze out more. Fine lamellar layers, a refined microstructure and increased dislocation density in ARB samples provide additional diffusion paths decreasing the reaction time.

Additional research proved that the annealing time can be further reduced. The HT duration for full Al consumption is between 1 h and 4 h

The binary Ti-Al phase diagram (Fig. 11) shows that compounds such as ordered intermetallic phases Ti_3Al, TiAl, $TiAl_2$, Ti_2Al_5 and $TiAl_3$ with a certain homogeneity range can be formed. The mechanisms of formation of intermetallic phases in the Ti/Al diffusion couple is still under discussion. Generally, it involves several steps: Diffusion, formation of saturated primary solid solutions, nucleation, growth of the nuclei and finally phase growth by consumption of adjacent phases. According to the phase diagram, the saturation state can be achieved very easily because the solubility of Al in Ti at 600°C is about 12 at.% [32], while Ti in Al is only about 0.55 at.% (confirmed by resistivity measurements [33] and electron probe microanalysis [34]).

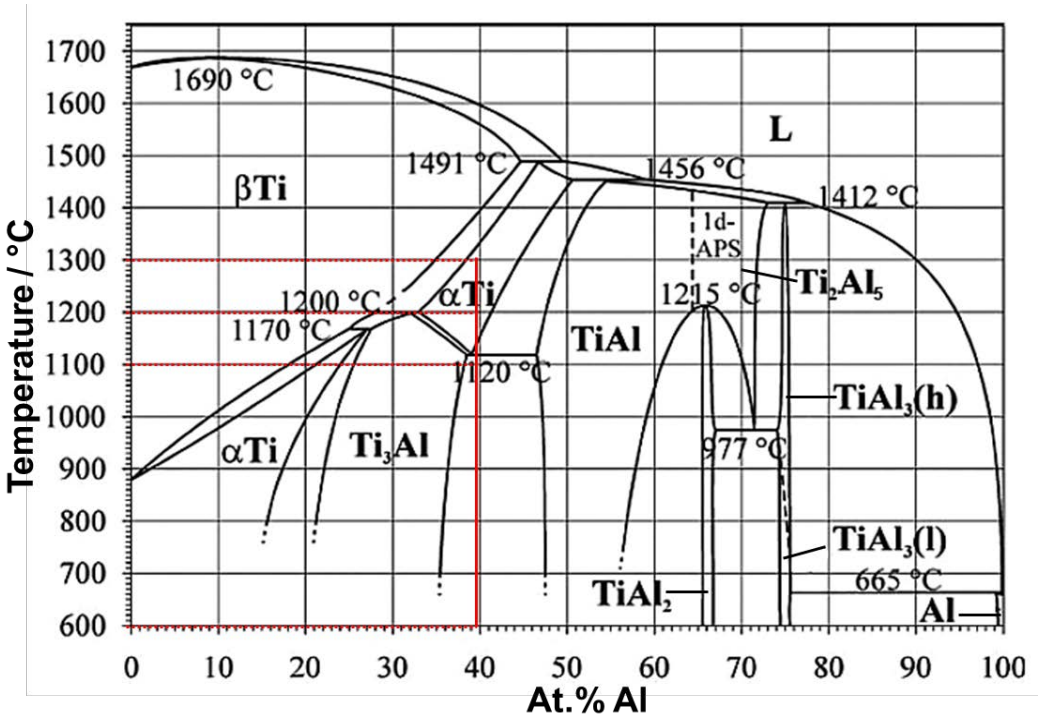

Fig. 11: Equilibrium phase diagram of the Ti-Al system according to Schuster [32]. The composition of the Ti-39.57 at.% Al and HT temperatures of 600°C, 1100°C, 1200°C and 1300°C are indicated with red lines.

In many previous publications involving solid-state Ti/Al reaction at temperatures below the melting point of aluminium it was observed that only $TiAl_3$ was formed [31, 35, 36, 37] or it was the dominant phase in the diffusion zone formed prior to the formation of any other Ti aluminides [38, 39]. In terms of thermodynamics, the possible reason for phase growth selection is the preference of Al-rich phases due to a low Gibbs free energy of formation. At 600°C $TiAl_3$ has the third lowest energy amongst the corresponding intermetallic phases.

However, $TiAl_2$ and Ti_2Al_5, which have the lowest free energy state, undergo a solid-state reaction with TiAl as one of the starting phases [40]. According to the effective heat of formation model proposed by Pretorius et al. [41, 42], standard heat of formation and effective concentration of Ti and Al at the reaction interface are considered for the estimation of free energy change during HT. $TiAl_3$ has the highest effective heat of formation and hence this compound is expected to form first at the interface. In addition to reasons for phase formation related to thermodynamics and diffusion dynamics, the ease of nucleation of $TiAl_3$ was explained by Tardy and Tu [43] in terms of similarities in the crystallographic structures of Al and $TiAl_3$.

Similarly, sintering of Ti/Al powder shows that only Ti_2Al_5 is formed after annealing at 450°C/24 h and is still present after 600°C/48 h HT. Therefore, it is assumed that the formation of $TiAl_3$ results from the reaction between solid Al and Ti_2Al_5 [44].

In the subsequent reaction process during HT2 at 1100°C the remaining titanium reacts to Ti_3Al, TiAl and $TiAl_2$. Because annealing at 1100°C does not lead to the complete disappearance of Al-rich phases, the annealing temperature was increased. Alternatively, a longer period of time would be needed for formation of a microstructure only consisting of TiAl and Ti_3Al. At 1200°C and 1300°C Al-rich phases disappear due to enhanced interdiffusion between Ti and Al, and only TiAl and Ti_3Al form.

4.2 Porosity

In the Ti/Al layered composites during pressureless HT a high level of porosity formation takes place. It can be caused by volume change due to the difference in molar volume between initial composition and product phases. When considering the amount of substance of the composition after pressureless HT of 36.3 vol.% Ti, 44.8 vol.% $TiAl_3$, 11.1 vol.% Ti_3Al, 6.2 vol.% TiAl, 0.8 vol.% $TiAl_2$ and 0.8 vol.% Ti_2Al_5, (state after pressureless HT1, see Fig. 4), the volume of the equivalent amount of pure Ti and Al is about 5% higher. Additionally, Kirkendall porosity forms during interdiffusion in the Ti/Al diffusion couple. To describe this in terms of experimental diffusion data, the impurity diffusion coefficient of Ti in Al is higher than Al in Ti at 600°C by three orders of magnitude ($D_{Ti} = 3 \times 10^{-17}$ m^2/s [45] and $D_{Al} = 4 \times 10^{-20}$ m^2/s [46]). Diffusivity depends on many parameters such as solute concentration, purity of solvent, grain size and crystal anisotropy [47, 48]. Nevertheless, the given values are consistent with the general correlation between solubility and diffusivity; atoms with lower solubility diffuse faster [49]. Consequently, during the initial interdiffusional mixing, the net flux of atomic diffusion of Ti into Al is higher. As mentioned above, the solubility of Ti in Al is about 22 times lower than that of Al in Ti. After

short initial interdiffusional mixing stage the saturation level of the solubility is reached and nucleation of $TiAl_3$ sets in. According to results on diffusion experiments in the Ti-Al system done by van Loo and Rieck [50], below 640°C Al is the dominant diffusing component in $TiAl_3$ causing a net flow of vacancies towards Al which then condense and form pores in the former elemental Al layers. As shown by theoretical calculations, the diffusion rate of Al (at 575°C) in the $TiAl_3$ phase exceeds about 20 times that of Ti ($D_{Ti} = 1.2 \times 10^{-15}$ m^2/s and $D_{Al} = 27.1 \times 10^{-15}$ m^2/s [51]).

The results show that applying pressure during HT1 has a significant influence on reducing large pores. By further increasing the pressure, the porosity remains relatively constant around 1 vol.% while the sample is flattened. As shown for sintered TiAl-based intermetallics, the use of a constraining die during HT prevents the change of sample dimensions and further reduction of the porosity [52].

Vacancy migration and dislocation climb play an important role in the reduction of porosity. Both effects are enhanced with increasing temperature and can be accelerated by applying an external pressure [53, 54]. Examination of the SEM images of samples heat-treated at 1100°C shows that probably due to Ostwald ripening the pores aggregate and coarsen but the layered structure of pores is preserved. At elevated temperatures (1200°C and 1300°C) increased diffusivity causes interconnected pores to further grow and become mostly elongated or spherical.

4.3 Sheet profiling

It has been demonstrated that sheet profiles of intermetallics consisting of TiAl and Ti_3Al can be fabricated by profiling the sheet in the as-ARB condition and applying the reaction annealings 1 and 2 with a certain pressure. The material outbreaks in the Al layers of the as-ARB sheet after bending may be explained as follows. The Al alloy used contains intermetallic precipitates which during bending lead to cracks at the interfaces with the Al solid solution matrix. These cracks easily lead to mechanical dislodging of the precipitates at the surface when preparing SEM cross sections. However, as the precipitate containing Al alloy is totally dissolved during reaction annealing the bending-induced cracks are of no relevance.

5. Conclusions

Accumulative roll bonded Ti/Al sheets were subjected to a two-step annealing treatment. Based on microstructural analysis by SEM, TEM and SR-XRD the following conclusions are drawn:

1) During annealing at 600°C for 12 h Al is completely consumed and $TiAl_3$ is the dominant intermetallic phase at the former Ti/Al interface. Additionally, pore formation inside the $TiAl_3$ layers occurs. The porosity of the ARB sheets is controlled by the Kirkendall effect and differences in molar volume of initial and product phases. The porosity is significantly reduced from 12 vol.% to about 1 vol.% by HT under a superimposed uniaxial pressure greater than 5 MPa.
2) A pressureless annealing at temperatures of 1100°C, 1200°C and 1300°C causes coarsening of the pores and an increase of the porosity up to about 3.8 vol.%. The temperature of 1100°C is not high enough for complete consumption of residual $TiAl_2$ and microstructural homogenization. During annealing at 1200°C and 1300°C sheets with duplex TiAl/Ti_3Al microstructure and slightly increased porosity are obtained. The porosity of final samples as a flat sheet and sheet profile can be substantially reduced down to 0.4 vol.% by applying an uniaxial pressure of about 100 MPa.
3) Oxidation occurs at elevated temperatures which entails the need of good oxidation protection.
4) It has been proven that the applied process is suitable for fabricating TiAl-based semi-finished material and therefore may be of technical relevance.

Acknowledgments

This research was funded by the Deutsche Forschungsgemeinschaft, DFG, project number SK 21/38-1.

References

[1] B.P. Bewlay, S. Nag, A. Suzuki, M.J. Weimer, TiAl alloys in commercial aircraft engines, Mater. High Temp. 33 (2016) 549-59.

[2] S. Djanarthany, J.C. Viala, J. Bouix, An overview of monolithic titanium aluminides based on Ti_3Al and TiAl, Mater. Chem. Phys. 72 (2001) 301-319.

[3] D.M. Dimiduk, D.B. Miracle, C.H. Ward, Development of intermetallic materials for aerospace systems, Mater. Sci. Technol. 8 (1992) 367-375.

[4] E.A. Loria, Quo vadis gamma titanium aluminide, Intermetallics 9 (2001) 997-1001.

[5] G. Baudana, S. Biamino, D. Ugues, M. Lombardi, P. Fino, M. Pavese, C. Badini, Titanium aluminides for aerospace and automotive applications processed by Electron Beam Melting, Met. Powd. Rep. 71 (2016) 193-199.

[6] J.P. Immarigeon, R.T. Holt, A.K. Koul, L. Zhao, W. Wallace, J.C. Beddoes, Lightweight materials for aircraft applications, Mater. Charact. 35 (1995) 41-67.

[7] W. Voice, The future of gamma-titanium aluminides by Rools Royce, Aircraft Eng. Aerospace Technol. 71 (1999) 337-340.

[8] H. Clemens, S. Mayer, Intermetallic titanium aluminides in aerospace applications – processing, microstructure and properties, Mater. High Temp. 33 (2016) 560-570.

[9] W. Chen, Z. Li, Additive manufacturing of titanium aluminides, Additive Manufacturing for the Aerospace Industry, Elsevier, 2019, 235-263.

[10} S.M.L. Sastry, H.A. Lipsitt, Plastic deformation of TiAl and Ti_3Al; Proc. 4th Int. Conf. on Titanium; Kyoto, Japan. 19-22 May 1980; pp. 1231-1243.

[11] Y.W. Kim, Ordered intermetallic alloys, part III: Gamma titanium aluminides, JOM-J. Min. Met. Mater. Soc. 46, (1994) 30-39.

[12] F.C. Campbell, Lightweight materials: Understanding the basics, ASM International (2012).

[13] Y.W. Kim, Effects of microstructure on the deformation and fracture of γ-TiAl alloys, Mater. Sci. Eng. A 192-193 (1995) 519-533.

[14] M. Burtscher, T. Klein, S. Mayer, H. Clemens, F.D. Fischer, The creep behaviour of a fully lamellar γ-TiAl based alloy, Intermetallics 114 (2019) 106611.

[15] D. Hu, J.F. Mei, M. Wickins, R.A. Hardy, Microstructure and tensile properties of investment cast TiAl–46Al–8Nb–1B alloy, Scr. Mater. 47 (2002) 273-278.

[16] M. Dahms, Formation of titanium aluminides by heat treatment of extruded elemental powders, Mater. Sci. Eng. A 110 (1989) L5-L8.

[17] M. Hsiung, T.G. Nieh, Microstructures and properties of powder metallurgy TiAl alloys, Mater. Sci. Eng. A 364 (2004) 1-10.

[18] A.A. Nepapushev, D.O. Moskovskikh, K. Vorotilo, A.S. Rogachev, TiAl-based materials by in situ selective laser melting of Ti/Al reactive composites, Metals 10 (2020) 1505.

[19] D.M. Fronczek, J. Wojewoda-Budka, R. Chulist, A. Sypien, A. Korneva, Z. Szulc, N. Schell, P. Zieba, Structural properties of Ti/Al clads manufactured by explosive welding and annealing, Mater. Des. 91 (2016) 80-89.

[20] W. Ge, C. Guo, F. Lin, Effect of Process Parameters on Microstructure of TiAl Alloy Produced by Electron Beam Selective Melting, Procedia Eng. 81 (2014) 1192-1197.

[21] G.P. Chaudhari, V.L. Acoff, Titanium aluminide sheets made using rolling bonding and reaction annealing, Intermetallics 18 (2010) 472-478.

[22] D. Yang, P. Hodgson, C. Wen, The kinetics of two-stage formation of $TiAl_3$ in multilayered Ti/Al foils prepared by accumulative roll bonding, Intermetallics 17 (2009) 727-732.

[23] J.G. Luo, V.L. Acoff, Using cold roll bonding and annealing to process Ti/Al multi-layered composites from elemental foils, Mater. Sci. Eng. A 379 (2004) 164-172.

[24] J. Romberg, J. Freudenberger, H. Bauder, G. Plattner, H. Krug, F. Holländer, J. Scharnweber, A. Eschke, U. Kühn, H. Klauß, C.-G. Oertel, W. Skrotzki, J. Eckert, L. Schultz, Ti/Al multi-layered sheets: accumulative roll bonding (Part A), Metals 6 (2016) 30.

[25] J. Scharnweber, P. Chekhonin, C.-G. Oertel, J. Romberg, J. Freudenberger, J. Jaschinski, W. Skrotzki, Microstructure, texture, and mechanical properties of laminar metal composites produced by accumulative roll bonding, Adv. Eng. Mater. 21 (2019) 1800210.

[26] Y.B. Sun, Y.Q. Zhao, D. Zhang, C. Liu, H.Y. Diao, C.L. Ma, Multilayered Ti-Al intermetallic sheets fabricated by cold rolling and annealing of titanium and aluminum foils, Trans. Nonferrous Met. Soc. China 21 (2011) 1722-1727.

[27] M. Nganbe, M. Heilmaier, High temperature strength and failure of the Ni-base superalloy PM 3030, Int. J. Plast. 25 (2009), 822-837.

[28] R. Chulist, L. Straka, H. Seiner, A. Sozinov, N. Schell, T. Tokarski, Branching of {110} twin boundaries in five-layered Ni-Mn-Ga bent single crystals, Mater. Des. 171 (2019) 107703.

[29] R. Chulist, P. Czaja, On the role of atomic shuffling in the 4O, 4M and 8M martensite structures in Ni-Mn-Sn single crystal, Scripta Mater. 189 (2020) 106-111.

[30] B. Batalu, G. Cosmeleata, A. Aloman, Critical analysis of the Ti-Al phase diagrams, U.P.B. Sci. Bull. B 68 (2006) 77-90.

[31] L. Xu, Y.Y. Cui, Y.L. Hao, R. Yang, Growth of intermetallic layer in multi-laminated Ti/Al diffusion couples, Mater. Sci. Eng. A 435, 2006, 638–647.

[32] J.C. Schuster, M. Palm, Reassessment of the binary aluminum-titanium phase diagram, J. Ph. Equil. and Diff. 27 (2006) 255-277.

[33] S. Hori, H. Tai, E. Matsumoto, Solid solubility of Titanium in aluminium, J. Jpn. Inst. Light Met. 34 (1984) 377-381.

[34] Y. Minamino, T. Yamane, H. Araki, N. Takeuchi, Y. –S. Kang, Y. Miyamoto, T. Okamoto, Solid solubilities of manganese and titanium in aluminium at 0.1 MPa and 2.1 GPa, Metall. Trans. 22A (1991) 783-786.

[35] F. Foadian, M. Soltanieh, M. Adeli, M. Etminanbakhs, A study on the formation of intermetallics during the heat treatment of explosively welded Ti-Al multilayers, Metall. Mater. Trans. A. 45 (2014) 1823-1832.

[36] M. Mirjalili, M. Soltanieh, K. Matsuura, M. Ohno, On kinetics of $TiAl_3$ formation during reaction synthesis from solid Ti and liquid Al, Intermetallics 32 (2013) 297-302.

[37] Y. Zhao, J. Li, R. Qiu, H. Shi, Growth characterization of intermetallic compound at the Ti/Al solid state interface, Materials 12 (2019) 472.

[38] A.H. Assari, B. Eghbali, Interfacial layers Evolution during annealing in Ti-Al multi-laminated composite processed using hot press and roll bonding, Met. Mater. Int. 22 (2016) 915-923.

[39] T. Marr, J. Freudenberger, A. Kauffmann, J. Romberg, I. Okulov, R. Petters, J. Scharnweber, A. Eschke, C.-G. Oertel, U. Kuhn, J. Eckert, W. Skrotzki, L. Schultz, Processing of intermetallic titanium aluminide wires, Metals 3 (2013) 188-201.

[40] A. Raman, K. Schubert, On the constitution of some alloy series related to $TiAl_3$. II. Investigations in some T4-Al-Si and T4...6-In systems, Z. Metallkd. 56 (1965) 44-52.

[41] R. Pretorius, R. De Reus, A.M. Vredenberg, F.W. Saris, Use of the effective heat of formation rule for predicting phase formation sequence in Al-Ni systems, Mater. Lett. 9 (1990) 494-499.

[42] R. Pretorius, A.M. Vredenberg, F.W. Saris, Prediction of phase formation sequence and phase stability in binary metal-aluminium thin-film system using the effective heat of formation rule, J. Appl. Phys 70 (1991) 3636-3646.

[43] J. Tardy, K.N. Tu, Solute effect of Cu on interdiffusion in Al_3Ti compound films, Phys. Rev. 32 (1985) 2070-2081.

[44] A. Školáková, P. Salvetr, J. Leitner, T. Lovaši, P. Novák. Formation of phases in reactively sintered $TiAl_3$ alloy, Molecules 25 (2020) 1912.

[45] D. Bergner, N. van Chi, Untersuchungen zur Diffusion von 3 d-Metallen in Al, Wiss. Zeitschrift der Pädagogischen Hochschule „N. K. Krupskaja“ Halle 15 (1977) 15.

[46] J. Räisänen, A. Anttila, J. Keinonen, Diffusion of aluminum in ion-implanted α-Ti, J. Appl. Phys 57 (1985) 613 – 614.

[47] M. Köppers, Chr. Herzig, M. Friesel, Y. Mishin, Intrinsic self-diffusion and substitutional Al diffusion in α-Ti, Acta Mat. 45 (1997) 4181-4191.

[48] D. H. St. John, L. M. Hogan, Thermal stability in the Al-Al_3Ti system, J. Mater. Sci. 15 (1980) 2369-2375.

[49] H. Nakajima, M. Koiwa, Diffusion in Titanium, ISIJ Int. 31 (1991) 757-766.

[50] F.J.J. van Loo, G.D. Rieck. Diffusion in the titanium-aluminium system. Interdiffusion between solid Al and Ti or Ti-Al alloys, Acta Metall. 21 (1973) 61-71.

[51] N. Thiyaneshwaran, K. Sivaprasad, B. Ravisankar, Nucleation and growth of $TiAl_3$ intermetallic phase in diffusion bonded Ti/Al metal intermetallic laminate, Sci. Rep. 8 (2018) 16797.

[52] J.B. Yang, W.S. Hwang, The preparation of TiAl-based intermetallics from elemental powders through a two-step pressureless sintering process. J. Mater. Eng. and Perform. 7 (1998) 385-392.

[53] G.-X. Wang, M. Dahms, Reaction sintering of cold-extruded elemental powder mixture Ti-48Al, Metall. Mater. Trans. A 24 (1993) 1517-1526.

[54] T.E. Volin, R.W. Balluffi, Annealing kinetics of voids and the self-diffusion coefficient in aluminium, Phys. Stat. Sol. (b) 25 (1968) 163-173.